

Constraining sub-eV Dark Matter from Direct Detection Experiments

Chen Xia,¹ Yan-Hao Xu,¹ and Yu-Feng Zhou^{1,2,3}

¹*CAS key laboratory of theoretical Physics, Institute of Theoretical Physics, Chinese Academy of Sciences, Beijing 100190, China. University of Chinese Academy of Sciences, Beijing, 100190, China.*

²*School of Fundamental Physics and Mathematical Sciences,*

Hangzhou Institute for Advanced Study, UCAS, Hangzhou 310024, China.

³*International Centre for Theoretical Physics Asia-Pacific, Beijing/Hangzhou, China.*

Light dark matter (DM) particles upscattered by high-energy cosmic rays (CRs) can be energetic, and become detectable by the conventional direct detection (DD) experiments. We show that if the energy spectrum of the primary CR flux follows a power law $\sim E^{-3}$, for constant cross sections, the upscattered DM flux will follow an universal power law of $\sim E^{-2}$ which is independent of DM particle mass m_χ . Consequently, the constraints on the DM-nucleon scattering cross section $\sigma_{\chi p}$ derived from DD experiments will be independent of m_χ as well, and can be formally extended to the limit of $m_\chi \rightarrow 0$. The fact that the observed primary CR flux is indeed very close to $\sim E^{-3}$ over many orders of magnitude, especially after the “knee” structure suggests that the current DD experiments are able to constrain ultralight DM far below eV scale. Using the ultrahigh-energy primary CR flux measured up to $\sim 10^{20}$ eV, we derive conservative constraints from the Xenon-1T data on the spin-independent cross section of $\sigma_{\chi p} \lesssim (10^{-32} - 10^{-31}) \text{ cm}^2$ for very small m_χ from $\sim \text{eV}$ down to $\sim 10^{-12}$ eV.

Introduction. Although compelling astrophysical evidence supports the existence of dark matter (DM) in the Universe, whether or not DM participates non-gravitational interactions is still unknown. The majority of the current direct detection (DD) experiments search for nuclear recoil signals from the scatterings between the halo DM particle χ and target nucleus N . As the typical threshold energy T_N^{thr} of the current DD experiments is $\sim \text{keV}$, searching for light sub-GeV halo DM particles is challenging. The reason is that for lighter halo DM particle the maximal kinetic energy is lower for a given escape velocity, and the energy transfer of the scattering process is less efficient. Some physical processes have been considered to reduce T_N^{thr} in the current experiments, such as bremsstrahlung [1] and the Migdal effect [2, 3], etc..

If DM particle can scatter off nucleus, the inverse process exists. For instance, high-energy cosmic-ray (CR) particles in the Galaxy can scatter off halo DM, which may lead to the energy loss of CR [4], production of γ -rays [5, 6], and energy boost of DM particles [7–9], etc.. In the last process, a small but irreducible component of DM (referred to as CRDM) can gain very high kinetic energy. These energetic CRDM particles can scatter again with the target nuclei in underground detectors, and deposit energy larger than T_N^{thr} , which makes them detectable, and greatly extend the sensitivity of the current DD experiments to light DM [7–14]. In the pioneering work adopting this strategy [7], it was shown that an upper limit on DM-nucleon scattering cross section of $\sigma_{\chi p} \leq 10^{-31} \text{ cm}^2$ can be obtained for CRDM particle mass m_χ down to at least ~ 0.1 MeV for constant cross sections (for the case of energy-dependent cross sections see. e.g. [10, 11]). It was also noticed in [7] that the obtained limits seemed to be insensitive to m_χ , and could be formally extended to vanishing m_χ , which raised an interesting possibility of constraining ultralight DM from

the current conventional DD experiments. However, the physical origin and validity of this m_χ insensitivity was not further explored. Furthermore, most analyses on the direct detection of CRDM [7–14] adopted parametrizations of primary CR (proton and Helium) fluxes [15] based on the space-based direct measurements such as AMS-02 [16, 17] and CREAM-I [18], etc., which are only available up to a few tens of TeV. Such parametrizations cannot be reliably extrapolated to higher energy to probe very light DM, as they failed to capture the important spectral features such as the “knee” and “ankle” in ultrahigh-energy CRs (UHECRs) (referred to CRs with energy $E \gtrsim 10^{15}$ eV). In this letter, we show that the validity of this approach is directly related to the power-law nature of the primary CR flux. If the primary CR flux is close to a power law $\sim E^{-3}$, for a constant scattering cross section, the upscattered DM flux will follow a power law of $\sim E^{-2}$, and the recoil event rate of DM-nucleus scattering follows a power law in recoil energy T_N as $\sim T_N^{-3/2}$. Both are independent of m_χ . Therefore the constraint on the DM-nucleon scattering cross section $\sigma_{\chi p}$ will be independent of m_χ as well. Note that the observed primary CR flux is indeed very close to $\sim E^{-3}$, especially above the “knee” structure, which suggests that the current DD experiments are able to constrain ultralight DM far below eV scale. Using the UHECR flux observed by ground-based air shower arrays, we derive upper limits of $\sigma_{\chi p} \lesssim 10^{-31} \text{ cm}^2$ for DM particle mass down to $m_\chi \sim 10^{-12}$ eV from the Xenon-1T data, which extends the constraints previously obtained in [7] by more than ten orders of magnitude towards lower DM mass.

kinematics. In the generic process of elastic scattering between an incident particle A with kinetic energy T_A and a target particle B at rest, the recoil energy of particle B in the laboratory frame is given by

$T_B = T_B^{\max}(1 - \cos\theta)/2$, where θ is the scattering angle of particle B in the center-of-mass (CM) frame. The maximal recoil energy of particle B is given by

$$\frac{T_B^{\max}}{T_A} = \left[1 + \frac{(m_B - m_A)^2}{2m_B(T_A + 2m_A)} \right]^{-1}, \quad (1)$$

where $m_{A(B)}$ is the mass of particle $A(B)$. We assume that the scattering is isotropic in the CM frame, such that the differential cross section $d\sigma_{AB}/dT_B$ in the laboratory frame is simply related to the total cross section σ_{AB} as $d\sigma_{AB}/dT_B = \sigma_{AB}/T_B^{\max}$. In the case of CR-DM scattering, the recoil energy of the DM particle upscattered by CR particles with species i ($i = \text{proton, He, } \dots$) can be obtained by setting $(A, B) = (i, \chi)$ in Eq. (1). In the case where the CR particle i is highly relativistic, i.e., the Lorentz factor $\gamma_i = T_i/m_i \gg 1$, but m_χ is small enough such that $\gamma_i \ll m_i/2m_\chi$, the maximal recoil energy of the CRDM can be approximated as

$$T_\chi^{\max} \approx 2m_\chi\gamma_i^2. \quad (2)$$

The CRDM particle with kinetic energy T_χ can scatter again with the nucleus N (with mass m_N) in either the outer crust of Earth or the detector of the underground DD experiments. The maximal recoil energy T_N^{\max} of the nucleus which is also the maximal energy-loss of CRDM particle, can be obtained from Eq. (1) by setting $(A, B) = (\chi, N)$. Since we are only interested in the case of light DM $m_\chi \ll m_N$, T_N^{\max} can be written as

$$T_N^{\max} = \frac{T_\chi^2 + 2m_\chi T_\chi}{T_\chi + m_N/2} \approx \frac{2T_\chi^2}{m_N}, \quad (3)$$

where the last step holds for $T_\chi \ll m_N$ which is the case most relevant to direct detection, as for too large T_χ the corresponding recoil energy T_N is outside detection range of the experiments. The combination of Eqs. (2) and (3) allows for an optimistic estimation on the lightest CRDM particle which can be detected by the DD experiments: So far the observed UHECR particles can have total energy up to $\sim 10^{20}$ eV per particle and are likely to be dominated by protons [19, 20]. Considering a typical target nucleus with mass $m_N \approx 100$ GeV and taking $T_\chi \approx T_\chi^{\max}$, we find that a CRDM particle with mass as low as $m_\chi \approx 10^{-15}$ eV can produce a recoil energy of $T_N^{\max} \sim$ keV, which is close to the threshold T_N^{thr} of the current DD experiments.

CRDM flux. After being upscattered, the CRDM particles travel through the Galaxy in straight lines as they are not deflected by the interstellar magnetic fields. The observed flux (number of particles per unit area, time and solid angle, $dN/dAdtd\Omega$) of CRDM at the surface of Earth can be approximately written as

$$\frac{d\Phi_\chi}{dT_\chi} \approx \frac{\rho_\chi^{\text{loc}} \sigma_{\chi i} D_{\text{eff}} F^2(Q_\chi^2)}{m_\chi} \int_{\gamma_i^{\min}(T_\chi)}^{\infty} \frac{d\gamma_i}{T_\chi^{\max}} \frac{d\Phi_i^{\text{LIS}}}{d\gamma_i}, \quad (4)$$

where $d\Phi_i^{\text{LIS}}/d\gamma_i$ is the local interstellar CR flux measured at Earth. The integration lower limit $\gamma_i^{\min} \approx (T_\chi/2m_\chi)^{1/2}$ is the minimal Lorentz factor required to produce T_χ , which can be obtained from inverting Eq. (2). The form factor $F(Q_\chi^2)$ is evaluated at the momentum transfer $Q_\chi^2 = 2m_\chi T_\chi$. In the above expression we have assumed that the CR energy spectrum in the Galactic halo is not significantly different from that in the local interstellar (LIS) region, i.e., $d\Phi_i(r)/d\gamma_i \approx d\Phi_i^{\text{LIS}}/d\gamma_i$. In this case, the information of halo DM density distribution can be parameterized into a single parameter $D_{\text{eff}} = \int_{\text{l.o.s.}} \rho_\chi / (4\pi\rho_\chi^{\text{loc}}) ds d\Omega$, where $\rho_\chi^{\text{loc}} \approx 0.3$ GeV/cm³ is the local DM density in the Solar system, and the integration is performed along the line-of-sight (l.o.s.). For typical DM profiles, the value of D_{eff} is around a few kpc. In this letter, we take a conservative value of $D_{\text{eff}} = 1$ kpc as a benchmark value.

Let us start with a simple scenario where the flux of a CR species i can be parametrized by a single power law with index α_i and a cutoff at a Lorentz factor $\gamma_{i,\text{cut}}$

$$\frac{d\Phi_i^{\text{LIS}}}{d\gamma_i} = \Phi_i^0 \gamma_i^{-\alpha_i} \exp\left(-\frac{\gamma_i}{\gamma_{i,\text{cut}}}\right), \quad (5)$$

where Φ_i^0 is a normalization factor. The power-law behavior is expected if CRs are accelerated by the diffusive shock waves of the Galactic supernova-remnants (SNRs) and the pulsar wind, etc., and the cutoff represents the maximal energy that can be achieved by the acceleration process. If m_χ is small enough such that $\gamma_{i,\text{cut}} \ll m_i/2m_\chi$ which is easily satisfied for sub-eV CRDM, the approximation of Eq. (2) is reasonable in the whole integration range, and the corresponding CRDM flux reads

$$\frac{d\Phi_\chi}{dT_\chi} = \frac{\sigma_{\chi i} \rho_\chi^{\text{loc}} D_{\text{eff}} \Phi_i^0 F^2}{2m_\chi^2 \gamma_{i,\text{cut}}^{\alpha_i+1}} \Gamma(-(\alpha_i + 1), t), \quad (6)$$

where Γ is the incomplete Γ -function, $t = (T_\chi/T_{\chi,\text{cut}}^{\max})^{1/2}$ with $T_{\chi,\text{cut}}^{\max} = 2m_\chi\gamma_{i,\text{cut}}^2$ the maximal energy of CRDM upscattered by UHECR at the cutoff $\gamma_{i,\text{cut}}$.

In the region far below the cutoff, i.e., $T_\chi \ll T_{\chi,\text{cut}}^{\max}$, the influence of the cutoff $\gamma_{i,\text{cut}}$ in the CR flux can be safely neglected, which reduces to the simple case where the CR flux is a single power law $\sim E^{-\alpha_i}$ with E the total energy. Using the asymptotic behavior of the incomplete Γ -function $\Gamma(a, z) \rightarrow -z^a/a$ for $z \ll 1$, the CRDM flux can be approximated as

$$\frac{d\Phi_\chi}{dT_\chi} \approx \frac{2\sigma_{\chi i} \rho_\chi^{\text{loc}} D_{\text{eff}} \Phi_i^0 F^2}{\alpha_i + 1} T_\chi^{-2} \left(\frac{T_\chi}{2m_\chi}\right)^{(3-\alpha_i)/2}, \quad (7)$$

which shows if $\alpha_i = 3$, the CRDM flux scales with energy as T_χ^{-2} , and becomes almost independent of m_χ , as $F(Q_\chi^2) \approx 1$ is a very good approximation for ultralight DM. Note that $\alpha_i = 3$ is fairly close to the reality. Direct and indirect measurements show that from a few GeV

up to the “knee” (at 3×10^{15} eV), the primary CR all-particle spectrum approximately follows a single power law with index $\alpha \approx 2.7$. Above the “knee” the spectrum softens to $\alpha \approx 3.1$, which is even closer to 3. Before reaching the highest energy $\sim 10^{20}$ eV, there are several minor spectral structures such as the “second knee” at $\sim 10^{17}$ eV, the “ankle” at $\sim 8 \times 10^{18}$ eV and the “toe” at $\sim 3 \times 10^{19}$ eV. The corresponding power-law indices vary around 3. Thus $d\Phi_\chi/dT_\chi$ in this ultrahigh-energy region should fluctuate around the power law T_χ^{-2} , and is highly insensitive to m_χ . Consequently, it is expected that the recoil event rate and the derived bounds on $\sigma_{\chi i}$ will be independent of m_χ as well, as from Eq. (3) the recoil energy or energy loss in the χN scattering does not depend on m_χ .

In a different region where T_χ is close to the cutoff $T_{\chi,\text{cut}}^{\text{max}}$, the effect of cutoff in CR flux will be significant. Using the asymptotic behavior of $\Gamma(a, z) \rightarrow z^{a-1}e^{-z}$ for large z , the CRDM flux is given by

$$\frac{d\Phi_\chi}{dT_\chi} \approx \frac{\sigma_{\chi i} \rho_\chi^{\text{loc}} D_{\text{eff}} \Phi_i^0 F^2}{2m_\chi^2 \gamma_{i,\text{cut}}^{\alpha_i+1}} \left(\frac{T_\chi}{T_{\chi,\text{cut}}^{\text{max}}} \right)^{-\frac{\alpha_i+2}{2}} e^{-\left(\frac{T_\chi}{T_{\chi,\text{cut}}^{\text{max}}} \right)^{1/2}}. \quad (8)$$

Since $T_{\chi,\text{cut}}^{\text{max}}$ is proportional to m_χ , in this region, the CRDM flux should depend significantly on m_χ . Most importantly, lighter CRDM particles will have an earlier cutoff. A final cutoff in the CR flux not far away from $\sim 10^{20}$ eV is expected from the inelastic scattering between UHECR particles and photons of the cosmic microwave background (CMB), as predicted by Greisen, Zatsepin and Kuzmin [21, 22] and is supported by recent observations [23–25]. The cutoff in the UHECR flux sets the scale of the minimal m_χ that can be detected by the DD experiments.

The observed primary CRs in the large energy range from GeV to 10^{20} eV may receive contributions from different sources such as SNRs, pulsar winds and active galactic nuclei (AGN), etc. (for recent reviews see e.g. [26–28]). Thus a realistic description of the CR flux naturally contain multiple components. In each component j ($j = 1, \dots, n$), the power index and cutoff for a CR species i could be different. The multiple component description is also essential to reproduce the spectral structure of UHECRs. Thus we adopt the following form of the primary CR flux [29]

$$\frac{d\Phi_i^{\text{LIS}}}{d\gamma_i} = \sum_{j=1}^n \Phi_{ij}^0 \gamma_i^{-\alpha_{ij}} \exp \left[-\frac{\gamma_i}{\gamma_{ij,\text{cut}}} \right], \quad (9)$$

where Φ_{ij}^0 and α_{ij} are the normalization factors and power indices, respectively, for a CR species i in the component j . Following the reasoning of Peters [30], the CR species in each component j should share a common cutoff in rigidity R_j , which leads to $\gamma_{ij,\text{cut}} = (Z_i/m_i)R_j$, where Z_i is the electric-charge of the CR species i . In [29] four different parametrization are found to be in good

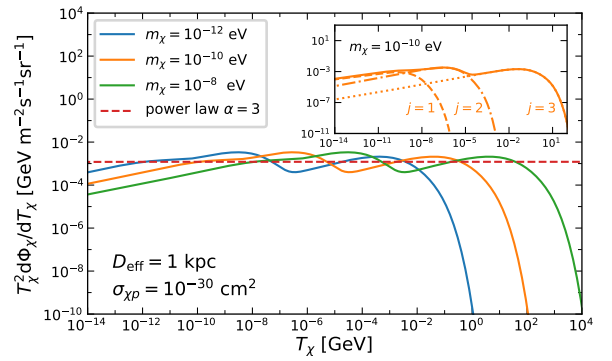


Figure 1. (solid lines) CRDM flux rescaled by T_χ^2 as a function of kinetic energy for different CRDM masses, for $\sigma_{\chi p} = 10^{-30}$ cm². The spectral structure in the flux is due to the three-component nature of the parametrization of CR [29]. The simple case where the CR is proton dominant and follows a single power-law with index $\alpha = 3$ and $\Phi^0 = 2.6 \times 10^2$ cm⁻²s⁻¹sr⁻¹ also shown (horizontal dashed line) for comparison. The inset shows the contribution from each CR component with $j = 1 - 3$ for the case of $m_\chi = 10^{-10}$ eV.

agreement with the data [23, 31–41]. We choose one of the “Global-Fit” parametrization with $n = 3$. The best-fit values of the rigidity cutoffs are $R_{1,2,3} = 120$ TV, 4 PV and 1.3 EV, respectively [29]. Compared with other parametrizations, this one is the most economic and conservative as the final cutoff of R_3 is the lowest, which leads to the lowest CRDM flux at high energies. The details of the parametrizations are summarized in the Supplementary Material.

Fig. 1 shows the CRDM flux calculated directly from Eqs.(1) and (4) without using any approximations. In the calculation we take the dipole form factors for light species H and He [42], and the Helm form factor for heavier species [43, 44]. As expected, in the energy region where T_χ is far below the lowest cut off, since $\alpha \approx 2.7$ the CRDM fluxes follow an approximate power law $\sim T_\chi^{-1.85}$ and scale with DM mass as $m_\chi^{-0.15}$ which is a rather weak m_χ -dependence. Thus lighter CRDM particle have slightly larger flux. In the cutoff dominated region, due to the superposition of various cutoffs $\gamma_{ij,\text{cut}}$ in the three components, the CRDM fluxes vary around the power law case of T_χ^{-2} and are insensitive to m_χ before reaching the last cutoff. Above the final cutoff, the CRDM flux drops rapidly, and the flux of lighter CRDM particle drops faster, as expected from Eq.(8).

Earth attenuation. Before reaching the underground detectors which typically located at a depth of ~ 1 km, the CRDM particle has to penetrate the outer crust of Earth, which may result in nonnegligible energy loss due to the scattering with the nucleus inside the crust. We adopt an analytic approach based on average energy loss [45, 46] which leads to conservative limits compared with numerical simulations [47, 48]. For simplicity, we only consider elastic scatterings which is an irreducible pro-

cess. The decrease of T_χ with depth z due to the elastic scattering with the nucleus N in Earth's crust is given by

$$\frac{dT_\chi}{dz} = - \sum_N \left(\frac{\rho_N}{m_N} \right) \int_0^{T_N^{\max}} T_N \frac{d\sigma_{\chi N}}{dT_N} dT_N, \quad (10)$$

where ρ_N is the mass density of nucleus N in the crust, and T_N stands for the nucleus recoil energy which equals the energy loss of the incident CRDM particle. Using the expression of T_N^{\max} in Eq. (3) the energy loss can be approximated as

$$\frac{dT_\chi}{dz} \approx -T_\chi^2 \sum_N \frac{\rho_N \sigma_{\chi N}}{m_N^2}. \quad (11)$$

Note that for highly relativistic CRDM, the energy loss is proportional to T_χ^2 and is independent of m_χ . In this letter, for simplicity we consider the case where the scattering is isospin conserving, namely, the cross section is the same for protons and neutrons inside the nucleus, $\sigma_{\chi n} = \sigma_{\chi p}$. For $m_\chi \ll m_p$, the cross section at the nucleon level and the nucleus level is simply related by the relation $\sigma_{\chi N} \approx A_N^2 \sigma_{\chi p}$ with A_N the nucleus mass number of N . We further adopt the approximation that the mass of the nucleus arises dominantly from the constituent nucleons, i.e., $m_N \approx A_N m_p$. Under these two simplifications, the factor A_N cancels out in Eq. (11), as $\sum_N \rho_N \sigma_{\chi N} / m_N^2 \approx \eta \sigma_{\chi p}$ with $\eta = \rho_\oplus / m_p^2$, where $\rho_\oplus \approx 2.7 \text{ g/cm}^3$ is the average density of Earth's outer crust [49]. Thus for light and relativistic CRDM, the effect of energy loss is also independent of the chemical composition of the crust. After integrating Eq. (11), the CRDM kinetic energy T_χ^z at depth z is related to that at surface as

$$\frac{T_\chi}{T_\chi^z} \approx \frac{1}{1 - \eta z T_\chi^z \sigma_{\chi p}}. \quad (12)$$

The CRDM flux $d\Phi_\chi/dT_\chi^z$ at depth z can be evaluated from that at surface $d\Phi_\chi/dT_\chi$ through the relation $d\Phi_\chi/dT_\chi^z = (d\Phi_\chi/dT_\chi)(dT_\chi/dT_\chi^z)$.

Direct detection. The recoil event rate per target nucleus mass $\Gamma = dN/dM_N dt dT_N$ of the χN scattering at depth z is given by

$$\Gamma = \frac{4\pi\sigma_{\chi N} F^2(Q_N^2)}{m_N} \int_{T_\chi^{z,\min}(T_N)}^\infty \frac{dT_\chi^z}{T_N^{\max}(T_\chi^z)} \frac{d\Phi_\chi}{dT_\chi^z}, \quad (13)$$

where $Q_N^2 = 2m_N T_N$. In deriving the exclusion regions from DD experiments, two extreme cases are of great importance. The one is where $\sigma_{\chi p}$ is small enough such that the effect of Earth attenuation is negligible, namely, $T_\chi^z \approx T_\chi$, which requires $\sigma_{\chi p} \ll (\eta z T_\chi^z)^{-1}$ from Eq.(12). The typical value of T_χ^z relevant to direct detection is set by $T_\chi^{z,\min}(T_N) \approx (T_N m_N / 2)^{1/2}$. For a typical detector located at depth $z \sim 1 \text{ km}$ with a target nucleus mass

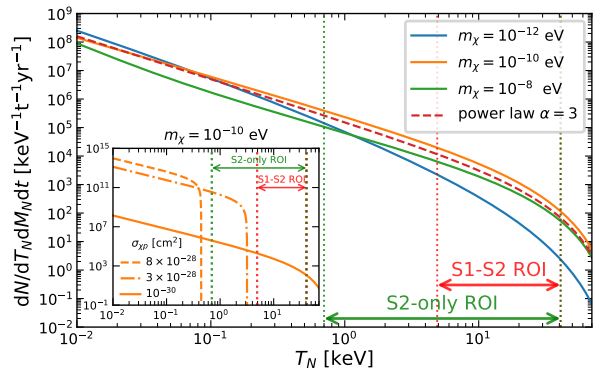


Figure 2. Recoil event rates of the scattering between CRDM particle and target Xenon nuclei with different DM masses. The value of $\sigma_{\chi p}$ and D_{eff} are the same as that in Fig. 1. The inset shows the recoil rate at different cross sections for $m_\chi = 10^{-10} \text{ eV}$. The vertical dotted lines indicate the ROIs considered by the Xenon-1T experiments for the S1-S2 and S2-only analyses.

$m_N \sim 100 \text{ GeV}$ and detection threshold $T_N^{\text{thr}} = 1 \text{ keV}$, in order to produce a recoil energy of $T_N \sim T_N^{\text{thr}}$, the required $T_\chi^{z,\min}$ is $\sim 10 \text{ MeV}$, which leads to a conservative requirement of $\sigma_{\chi p} \ll \mathcal{O}(10^{-27}) \text{ cm}^2$. Since the lower bounds of the excluded cross section is expected to be $\sigma_{\chi p} < 10^{-30} \text{ cm}^2$ [7], in deriving the lower bound of the excluded cross section, the effect of Earth attenuation can be safely neglected. Using the CRDM flux and $F^2(Q_\chi) \approx 1$ in Eq. (6), the recoil event rate after integration of Eq. (13) is given by

$$\Gamma \approx \frac{\pi\sigma_{\chi N}\sigma_{\chi p}\rho_\chi D_{\text{eff}}\Phi_\chi^0 F^2(Q_N^2)}{2m_\chi^3 \gamma_{i,\text{cut}}^{\alpha_i+3}} \times \left[-\Gamma(-3 - \alpha_i, t') + \frac{\Gamma(-1 - \alpha_i, t')}{t'^2} \right], \quad (14)$$

where $t' = [T_\chi^{\min}(T_N)/T_\chi^{\text{cut}}]^{1/2}$. In the case where $t' \ll 1$, namely, the effect of the cutoff is negligible, the recoil event rate can be approximated as

$$\Gamma \approx \frac{\pi\sigma_{\chi N}\sigma_{\chi p}\rho_\chi D_{\text{eff}}\Phi_\chi^0 F^2}{(1 + \alpha_i)(3 + \alpha_i)m_N^3} \left(\frac{m_N}{m_\chi} \right)^{\frac{3-\alpha_i}{2}} \left(\frac{T_N}{8m_N} \right)^{-\frac{3+\alpha_i}{4}},$$

which explicitly shows that in the limit of $\alpha_i = 3$, the recoil event rate is proportional to $T_N^{-3/2}$ and independent of m_χ . Consequently, the derived upper limit on $\sigma_{\chi p}$ will be independent of m_χ as well. In Fig. 2, we show the recoil event rate of the scattering between the CRDM particles and xenon nuclei. The approximate power-law behavior of the recoil spectrum can be clearly seen for $T_N \lesssim \text{keV}$. Above $\sim 10 \text{ keV}$, the suppression due to the Helm form factor is visible. In the figure, we also show the energy region-of-interests (ROIs) in which the Xenon-1T experiment performed signal searches, which is $4.9\text{--}40.9 \text{ keV}_{\text{nr}}$ for S1-S2 analysis [50] and $0.7\text{--}40.9 \text{ keV}_{\text{nr}}$

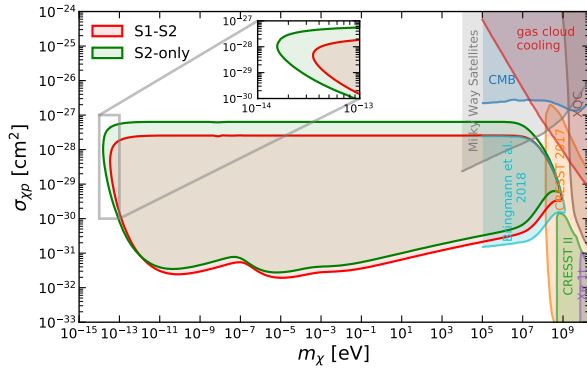


Figure 3. Exclusion regions in the $(m_\chi, \sigma_{\chi p})$ plane derived from the Xenon-1T data on the S1-S2 signals and S2-only signals. The constraints from other experiments such as Xenon-1T [50, 55], CRESST-II [56], CRESST surface run [57], XQC [58] and CMB [59], gas cloud cooling [60], Milky way satellite population [61] and the result of Bringmann, et al. [7] are also shown for comparison.

for S2-only analysis [51]. Due to the power-law like spectrum of the recoil event rate, the detection of CRDM is sensitive to the threshold T_N^{thr} . The experiment with lower T_N^{thr} is more sensitive to smaller m_χ .

The other case is where the cross section $\sigma_{\chi p}$ is large enough such that T_χ^z stops tracking the increase of T_χ , and will reach a maximal value $T_\chi^{z, \text{max}} \approx (\eta \sigma_{\chi p} z)^{-1}$ from Eq. (12). The appearance of $T_\chi^{z, \text{max}}$ is related to the fast energy loss proportional to T_χ^2 for relativistic particles, which leads to a cutoff of the CRDM flux. If the corresponding maximal recoil energy from Eq. (3) is below the threshold T_N^{thr} , it will form a blind spot for direct detection, which is illustrated in the inset of Fig. 2. Note that the correspond critical cross section $\sigma_{\chi p}$ is also independent of m_χ .

We derive excluded regions in the $(m_\chi, \sigma_{\chi p})$ plane at 90% C.L. for CRDM from the data of Xenon-1T experiment located at depth $z \approx 1.4$ km [50, 51]. Since the nuclear recoil event rate from the collisions with CRDM is quite different from that with the nonrelativistic halo DM, we derive the limits directly from the distribution of the signals of prompt scintillation (S1) and ionization electron (S2), rather than naively rescaling the reported Xenon-1T limits from WIMP searches. For the calculations from the deposited recoil energy T_N to the position-corrected signals cS1 and cS2_b, we closely follow Ref. [52]. To be conservative, the exclusion regions were derived using the binned Poisson statistic approach [53, 54], which are shown in Fig. 3. The calculation procedure, main parameters and excluded regions with different parametrizations of CR flux are summarized in the Supplementary Material. It can be seen that the lower bound of the excluded region reaches $\sigma_{\chi p} \lesssim 10^{-31}$ cm² in a large CRDM mass range $m_\chi \sim (10^{-12} - 1)$ eV. In this region, the shape of the excluded region is directly related to the

structure in the UHECR flux. For instance, the most stringent limit of $\sigma_{\chi p} \lesssim 3 \times 10^{-32}$ cm² at $m_\chi \sim 10^{-11}$ eV and 10^{-5} eV corresponds to the “knee” and the “toe” structure of the primary CR flux. The exclusion region closes at $m_\chi \sim 10^{-14}$ eV, which corresponds to the observed suppression of the CR flux at $\sim 10^{20}$ eV. The constraints on the lowest CRDM mass is sensitive to the detector threshold. Due to the lower threshold of the S2-only data, the constraints from the S2-only data which has an exposure much smaller than that of the S1-S2 data turns out to be more sensitive to lighter CRDM below 10^{-12} eV, as it can be seen in the inset of Fig. 3. The upper bound of the excluded region due to the Earth attenuation is found to be $\sigma_{\chi p} \lesssim 8 \times 10^{-28}$ cm², and is almost insensitive to m_χ , as expected from the fast energy loss proportional to T_χ^2 in Earth attenuation. Note that the constraints obtained in this approach is highly model independent. For ultralight DM particles there exists very stringent constraints, if they can reach thermal equilibrium during the epoch of big bang nucleosynthesis [11, 62]. These constraints, however, depend on models connecting DM scattering and annihilation or decay.

Conclusions. We have shown that the current DD experiments can place stringent constraints on the scattering cross section $\sigma_{\chi p}$ for ultralight DM upscattered by UHECRs, which is related to the unique spectral feature of primary CRs. The constraints on $\sigma_{\chi p}$ derived in this letter is complementary to that derived from the observations of CMB [59, 63–65], Lyman- α forest [66] and 21 cm radiations [63] from different epochs of the Universe.

We are grateful to Qian Yue and Li-Tao Yang for helpful discussions. This work is supported in part by The National Key R&D Program of China No. 2017YFA0402204 and by the National Natural Science Foundation of China (NSFC) No. 11825506, No. 11821505, No. U1738209, No. 11851303 and No. 11947302.

-
- [1] C. Kouvaris and J. Pradler, Phys. Rev. Lett. **118**, 031803 (2017), arXiv:1607.01789 [hep-ph].
 - [2] M. Ibe, W. Nakano, Y. Shoji, and K. Suzuki, JHEP **03**, 194 (2018), arXiv:1707.07258 [hep-ph].
 - [3] M. J. Dolan, F. Kahlhoefer, and C. McCabe, Phys. Rev. Lett. **121**, 101801 (2018), arXiv:1711.09906 [hep-ph].
 - [4] C. V. Cappiello, K. C. Ng, and J. F. Beacom, Phys. Rev. D **99**, 063004 (2019), arXiv:1810.07705 [hep-ph].
 - [5] R. H. Cyburt, B. D. Fields, V. Pavlidou, and B. D. Wandelt, Phys. Rev. D **65**, 123503 (2002), arXiv:astro-ph/0203240.
 - [6] D. Hooper and S. D. McDermott, Phys. Rev. D **97**, 115006 (2018), arXiv:1802.03025 [hep-ph].
 - [7] T. Bringmann and M. Pospelov, Phys. Rev. Lett. **122**, 171801 (2019), arXiv:1810.10543 [hep-ph].
 - [8] Y. Ema, F. Sala, and R. Sato, Phys. Rev. Lett. **122**, 181802 (2019), arXiv:1811.00520 [hep-ph].
 - [9] C. Cappiello and J. F. Beacom, Phys. Rev. D **100**, 103011

- (2019), arXiv:1906.11283 [hep-ph].
- [10] J. B. Dent, B. Dutta, J. L. Newstead, and I. M. Shoemaker, *Phys. Rev. D* **101**, 116007 (2020), arXiv:1907.03782 [hep-ph].
- [11] K. Bondarenko, A. Boyarsky, T. Bringmann, M. Hufnagel, K. Schmidt-Hoberg, and A. Sokolenko, *JHEP* **03**, 118 (2020), arXiv:1909.08632 [hep-ph].
- [12] W. Wang, J.-J. Wu, Z.-H. Xiong, and J. Zhao, *Chin. Phys. C* **44**, 063102 (2020), arXiv:1912.12594 [hep-ph].
- [13] S.-F. Ge, J.-L. Liu, Q. Yuan, and N. Zhou, (2020), arXiv:2005.09480 [hep-ph].
- [14] B.-L. Zhang, Z.-H. Lei, and J. Tang, (2020), arXiv:2008.07116 [hep-ph].
- [15] S. Della Torre *et al.*, in *25th European Cosmic Ray Symposium* (2016) arXiv:1701.02363 [astro-ph.HE].
- [16] M. Aguilar *et al.* (AMS), *Phys. Rev. Lett.* **114**, 171103 (2015).
- [17] M. Aguilar *et al.* (AMS), *Phys. Rev. Lett.* **119**, 251101 (2017).
- [18] Y. Yoon *et al.*, *Astrophys. J.* **728**, 122 (2011), arXiv:1102.2575 [astro-ph.HE].
- [19] Y. Tameda (Telescope Array, HiRes), *EPJ Web Conf.* **53**, 04005 (2013).
- [20] R. Abbasi *et al.* (HiRes), *Phys. Rev. Lett.* **104**, 161101 (2010), arXiv:0910.4184 [astro-ph.HE].
- [21] K. Greisen, *Phys. Rev. Lett.* **16**, 748 (1966).
- [22] G. T. Zatsepin and V. A. Kuzmin, *JETP Lett.* **4**, 78 (1966).
- [23] R. Abbasi *et al.* (HiRes), *Phys. Rev. Lett.* **100**, 101101 (2008), arXiv:astro-ph/0703099.
- [24] A. Castellina (Pierre Auger), *PoS ICRC2019*, 004 (2020), arXiv:1909.10791 [astro-ph.HE].
- [25] O. Deligny (Pierre Auger, Telescope Array), *PoS ICRC2019*, 234 (2020), arXiv:2001.08811 [astro-ph.HE].
- [26] M. Kachelriess and D. Semikoz, *Prog. Part. Nucl. Phys.* **109**, 103710 (2019), arXiv:1904.08160 [astro-ph.HE].
- [27] A. A. Watson, *Rept. Prog. Phys.* **77**, 036901 (2014), arXiv:1310.0325 [astro-ph.HE].
- [28] M. Nagano and A. A. Watson, *Rev. Mod. Phys.* **72**, 689 (2000).
- [29] T. K. Gaisser, T. Stanev, and S. Tilav, *Front. Phys. (Beijing)* **8**, 748 (2013), arXiv:1303.3565 [astro-ph.HE].
- [30] Peters, *Il Nuovo Cim.* **XXII**, 800-819 (1961).
- [31] M. Nagano, M. Teshima, Y. Matsubara, H. Dai, T. Hara, N. Hayashida, M. Honda, H. Ohoka, and S. Yoshida, *J. Phys. G* **18**, 423 (1992).
- [32] M. Glasmacher *et al.*, *Astropart. Phys.* **10**, 291 (1999).
- [33] F. Arqueros *et al.* (HEGRA), *Astron. Astrophys.* **359**, 682 (2000), arXiv:astro-ph/9908202.
- [34] M. Takeda *et al.*, *Astropart. Phys.* **19**, 447 (2003), arXiv:astro-ph/0209422.
- [35] T. Antoni *et al.* (KASCADE), *Astropart. Phys.* **24**, 1 (2005), arXiv:astro-ph/0505413.
- [36] M. Amenomori *et al.* (TIBET III), *Astrophys. J.* **678**, 1165 (2008), arXiv:0801.1803 [hep-ex].
- [37] M. Aartsen *et al.* (IceCube), *Phys. Rev. D* **88**, 042004 (2013), arXiv:1307.3795 [astro-ph.HE].
- [38] S. Ter-Antonyan, *Phys. Rev. D* **89**, 123003 (2014), arXiv:1405.5472 [astro-ph.HE].
- [39] V. Prosin *et al.*, *EPJ Web Conf.* **121**, 03004 (2016).
- [40] F. Fenu (Pierre Auger), *PoS ICRC2017*, 486 (2018).
- [41] C. J. Arteaga-Velázquez *et al.* (KASCADE Grande), *PoS ICRC2017*, 316 (2018).
- [42] C. Perdrisat, V. Punjabi, and M. Vanderhaeghen, *Prog. Part. Nucl. Phys.* **59**, 694 (2007), arXiv:hep-ph/0612014.
- [43] R. H. Helm, *Phys. Rev.* **104**, 1466 (1956).
- [44] J. Lewin and P. Smith, *Astropart. Phys.* **6**, 87 (1996).
- [45] C. Kouvaris and I. M. Shoemaker, *Phys. Rev. D* **90**, 095011 (2014), arXiv:1405.1729 [hep-ph].
- [46] G. D. Starkman, A. Gould, R. Esmailzadeh, and S. Dimopoulos, *Phys. Rev. D* **41**, 3594 (1990).
- [47] T. Emken, C. Kouvaris, and I. M. Shoemaker, *Phys. Rev. D* **96**, 015018 (2017), arXiv:1702.07750 [hep-ph].
- [48] T. Emken and C. Kouvaris, *JCAP* **10**, 031 (2017), arXiv:1706.02249 [hep-ph].
- [49] R. Rudnick and S. Gao, *Composition of the continental crust*, in *Treatise on Geochemistry*, Pergamon, Oxford, 2003.DOI:10.1016/B0-08-043751-6/03016-4.
- [50] E. Aprile *et al.* (XENON), *Phys. Rev. Lett.* **121**, 111302 (2018), arXiv:1805.12562 [astro-ph.CO].
- [51] E. Aprile *et al.* (XENON), *Phys. Rev. Lett.* **123**, 251801 (2019), arXiv:1907.11485 [hep-ex].
- [52] E. Aprile *et al.* (XENON), *Phys. Rev. D* **99**, 112009 (2019), arXiv:1902.11297 [physics.ins-det].
- [53] A. M. Green, *Phys. Rev. D* **65**, 023520 (2002), arXiv:astro-ph/0106555.
- [54] C. Savage, G. Gelmini, P. Gondolo, and K. Freese, *JCAP* **04**, 010 (2009), arXiv:0808.3607 [astro-ph].
- [55] E. Aprile *et al.* (XENON), *Phys. Rev. Lett.* **123**, 241803 (2019), arXiv:1907.12771 [hep-ex].
- [56] G. Angloher *et al.* (CRESSST), *Eur. Phys. J. C* **76**, 25 (2016), arXiv:1509.01515 [astro-ph.CO].
- [57] G. Angloher *et al.* (CRESSST), *Eur. Phys. J. C* **77**, 637 (2017), arXiv:1707.06749 [astro-ph.CO].
- [58] M. S. Mahdawi and G. R. Farrar, *JCAP* **10**, 007 (2018), arXiv:1804.03073 [hep-ph].
- [59] W. L. Xu, C. Dvorkin, and A. Chael, *Phys. Rev. D* **97**, 103530 (2018), arXiv:1802.06788 [astro-ph.CO].
- [60] A. Bhoonah, J. Bramante, F. Elahi, and S. Schon, *Phys. Rev. Lett.* **121**, 131101 (2018), arXiv:1806.06857 [hep-ph].
- [61] E. O. Nadler, V. Gluscevic, K. K. Boddy, and R. H. Wechsler, *Astrophys. J. Lett.* **878**, 32 (2019), [Erratum: *Astrophys.J.Lett.* 897, L46 (2020), Erratum: *Astrophys.J.* 897, L46 (2020)], arXiv:1904.10000 [astro-ph.CO].
- [62] G. Krnjaic and S. D. McDermott, *Phys. Rev. D* **101**, 123022 (2020), arXiv:1908.00007 [hep-ph].
- [63] T. R. Slatyer and C.-L. Wu, *Phys. Rev. D* **98**, 023013 (2018), arXiv:1803.09734 [astro-ph.CO].
- [64] V. Gluscevic and K. K. Boddy, *Phys. Rev. Lett.* **121**, 081301 (2018), arXiv:1712.07133 [astro-ph.CO].
- [65] K. K. Boddy and V. Gluscevic, *Phys. Rev. D* **98**, 083510 (2018), arXiv:1801.08609 [astro-ph.CO].
- [66] R. Murgia, V. Iršič, and M. Viel, *Phys. Rev. D* **98**, 083540 (2018), arXiv:1806.08371 [astro-ph.CO].
- [67] H. Ahn *et al.* (CREAM), *Astrophys. J. Lett.* **714**, L89 (2010), arXiv:1004.1123 [astro-ph.HE].
- [68] O. Adriani *et al.* (PAMELA), *Science* **332**, 69 (2011), arXiv:1103.4055 [astro-ph.HE].
- [69] T. K. Gaisser, *Astropart. Phys.* **35**, 801 (2012), arXiv:1111.6675 [astro-ph.HE].
- [70] A. Hillas, *J. Phys. G* **31**, R95 (2005).
- [71] B. Lenardo, K. Kazkaz, A. Manalaysay, J. Mock, M. Szydagis, and M. Tripathi, *IEEE Trans. Nucl. Sci.* **62**, 3387 (2015), arXiv:1412.4417 [astro-ph.IM].

- [72] J. Thomas and D. Imel, *Phys. Rev. A* **36**, 614 (1987).
- [73] M. Szydagis, N. Barry, K. Kazkaz, J. Mock, D. Stolp, M. Sweany, M. Tripathi, S. Uvarov, N. Walsh, and M. Woods, *JINST* **6**, P10002 (2011), arXiv:1106.1613 [physics.ins-det].
- [74] A. Drukier, K. Freese, and D. Spergel, *Phys. Rev. D* **33**, 3495 (1986).
- [75] W. A. Rolke, A. M. Lopez, and J. Conrad, *Nucl. Instrum. Meth. A* **551**, 493 (2005), arXiv:physics/0403059.
- [76] E. Aprile *et al.* (XENON), *Phys. Rev. D* **100**, 052014 (2019), arXiv:1906.04717 [physics.ins-det].

(Supplementary Material) Constraining sub-eV Dark Matter from Direct Detection Experiments

Chen Xia, Yan-Hao Xu, and Yu-Feng Zhou

In this supplementary material we give the details of the UHECR flux parametrization and the Xenon-1T signal analysis related to the results in the main text. We also provide extended results on the constraints on the CRDM-nucleon scattering cross section for different parametrizations of the UHECR flux.

I. PARAMETRIZATIONS OF UHECR FLUX

CR particles with energy above a few hundred TeV are mainly measured by the ground-based air-shower arrays which detect the cascades of secondary particles from the interactions of primary CR particles in the Earth atmosphere. In such indirect experiments, the information about the chemical composition is limited to determining the relative abundance of the main species or groups. Thus, it is likely that there exists different parametrizations which can describe the data equally well. We take the n -component power-law parametrization in which the CR total energy spectrum of the CR species i has the following form [29]

$$\frac{d\Phi_i^{\text{LIS}}}{dE_i} = \sum_{j=1}^n c_{ij} E_i^{-\alpha_{ij}} \exp\left[-\frac{E_i}{Z_i R_j}\right], \quad (\text{S-1})$$

where $j = (1, \dots, n)$ is the component index, E_i (in unit of GeV) is the total energy of CR species i . The normalization constants c_{ij} are related to Φ_{ij}^0 in Eq. (5) of the main text by $\Phi_{ij}^0 = m_i^{1-\alpha_{ij}} c_{ij}$ where m_i (in unit of GeV) is the mass of CR species i . A global analysis to the recent UHECR data has been performed in [29]. We adopt one of the three-component ‘‘Global-Fit’’ model as the benchmark model with the parameters listed in Table S-1. In this parametrization, the first rigidity cutoff R_i is around 100 TV which is the typical maximal energy from the acceleration of SNR with magnetic field around a few μ Gauss. It also well reproduce the observed hardening in the CR all-particle spectrum above 200 GeV [67, 68]. In the figure, we also list a slightly extended four-component parametrization (referred to as ‘‘Global-Fit4’’).

		p	He	C	O	Fe	50<Z<56	78<Z<82
$R_1 = 120$ TV	c_{i1}	7000	3200	100	130	60		
	α_{i1}	2.66	2.58	2.4	2.4	2.3		
$R_2 = 4$ PV	c_{i2}	150	65	6	7	2.3 (2.1)	0.1	0.4 (0.53)
	α_{i2}	2.4	2.3	2.3	2.3	2.2	2.2	2.2
$R_3 = 1.3$ EV	c_{i3}	14 (12)				0.025 (0.011)		
	α_{i3}	2.4				2.2		
$(R_4 = 40$ EV)	c_{i4}	(1.2)						
	α_{i4}	(2.4)						

Table S-1. Normalization constants c_{ij} , power indexes α_{ij} , and rigidity cutoffs R_j in the parametrization of ‘‘Global-Fit’’ and ‘‘Global-Fit4’’ in [29]. The parameters of ‘‘Global-Fit4’’ which are different from those of the ‘‘Global-Fit’’ are shown in parentheses.

Two alternative parametrizations [69] based on the Hillas model [70] are also found in good agreement with data, which are labeled as ‘‘H3a’’ and ‘‘H4a’’ in [29]. The major difference from the ‘‘Global-Fit’’ parametrization is that the first rigidity cutoff is quite high about 4 PV, which is responsible for the ‘‘knee’’ structure. In this type of parametrization the ‘‘ankle’’ represent the transition between the galactic and extra-galactic contributions. The corresponding parameters are listed in Table S-2.

The CR all-particle fluxes of the four parametrizations are shown in Figure S-1 together with the recent experiments data.

		p	He	CNO	Mg-Si	Fe
$R_1 = 4$ PV	c_{i1}	7860	3550	2200	1430	2120
	α_{i1}	2.66	2.58	2.63	2.67	2.63
$R_2 = 30$ PV	c_{i2}	20	20	13.4	13.4	13.4
	α_{i2}	2.4	2.4	2.4	2.4	2.4
$R_3 = 2$ (60) EV	c_{i3}	1.7 (200)	1.7 (0.0)	1.14 (0.0)	1.14 (0.0)	1.14 (0.0)
	α_{i3}	2.4 (2.6)	2.4	2.4	2.4	2.4

Table S-2. Same as Table S-1, but for parametrizations of “H3a” and “H4a” in [29]. The parameters of “H4a” which are different from those of “H3a” are shown in parentheses.

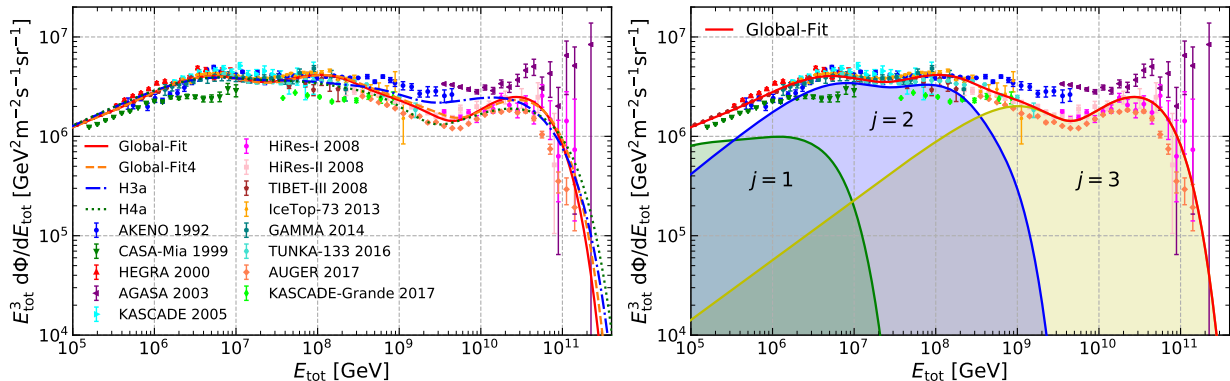


Figure S-1. Left) CR all-particle spectra for four type of parametrizations in [29] together with the current experimental data [23, 31–41] Right) Contributions from the three individual components in the “Global-Fit” parametrization in [29]

II. XENON-1T DATA ANALYSIS

For the data analysis of the Xenon-1T experiment, we adopt the signal response model described by the Xenon-1T collaboration in [52]. The Xenon-1T experiment utilizes the liquid xenon time projection chambers to detect the recoil energy of the target nuclei from the scattering with DM particles. The deposited energy can produce a prompt scintillation light signal (S1), and the ionization electrons extracted from liquid xenon into gaseous xenon can produce proportional scintillation light (S2). The S2/S1 signal size ratio allows for discrimination between nuclear recoil (NR) and electron recoil (ER) events. For a deposited recoil energy T_N , the produced total number of quantum N_q is the sum of the number of excitons N_{ex} and ion-electron pairs N_i , which follows a binomial distribution $N_q \sim \text{Binom}(T_N/W, L)$ where $W = 13.8$ eV is the average energy required to create either an exciton or ion-electron pair in the liquid xenon, and L is the Lindhard factor. In the case of NR, it is given by [71]

$$L = \frac{k g(\epsilon)}{1 + k g(\epsilon)}, \quad (\text{S-2})$$

where k is a normalization factor, the function $g(\epsilon)$ is proportional to the ratio of electric and nuclear stopping power, which can be parametrized as $g(\epsilon) = 3\epsilon^{0.15} + 0.7\epsilon^{0.6} + \epsilon$, where $\epsilon = 11.5(T_N/\text{keV})Z^{-7/3}$ with $Z = 54$ the atomic number of the xenon nucleus. The distribution of N_i is described by a binomial distribution $N_i \sim \text{Binom}(N_q, 1/(1 + \langle N_{ex}/N_i \rangle))$, where $\langle N_{ex}/N_i \rangle$ is the averaged exciton-to-ion ratio. The number of excitons is given by $N_{ex} = N_q - N_i$. The excitons contribute to scintillation photon signals through de-excitation process. The ionized electrons have a probability of r to be recombined into xenon atoms and produce scintillation photons, and a probability of $(1 - r)$ to escape the ion-electron pair. Thus the number of escaped electrons is given by $N_e \sim \text{Binom}(N_i, 1 - r)$ and the total number of photons is $N_\gamma = N_{ex} + N_i - N_e$. The recombination probability r is modeled by a Gaussian distribution $r \sim \text{Gauss}(\langle r \rangle, \Delta r)$, where $\langle r \rangle$ is the mean value and Δr is the variance. The mean value is calculated using the Thomas-Imel box model [72, 73]

$$\langle r \rangle = 1 - \frac{\ln(1 + N_i S/4)}{N_i S/4}, \quad (\text{S-3})$$

where $\varsigma = 0.057F^{-0.12}$ with F the electric field (in V/cm). The variance is described by $\Delta r = q_2(1 - e^{-T_N/q_3})$ with $q_2 = 0.034$ and $q_3 = 1.7$. In summary, the averaged number of photons $\langle N_\gamma \rangle$ and charges $\langle N_e \rangle$ are given by

$$\begin{aligned}\frac{\langle N_\gamma \rangle}{T_N} &= \frac{L}{W} \cdot \frac{\langle r \rangle + \langle N_{ex}/N_i \rangle}{1 + \langle N_{ex}/N_i \rangle}, \\ \frac{\langle N_e \rangle}{T_N} &= \frac{L}{W} \cdot \frac{1 - \langle r \rangle}{1 + \langle N_{ex}/N_i \rangle}.\end{aligned}\tag{S-4}$$

The photon and charge signals are converted into photoelectron (PE) emission of the photomultiplier tube (PMT) photocathode. The corresponding gain factors are: $g'_1(x, y, z)$ the average number of PEs observed per emitted photon, and $g'_2(x, y)$ the amplification factor for charge signals. Both are spatial dependent.

The spatial-dependence of the signals S1 and S2 are corrected, which results in the corrected signals cS1 and cS2_b (corresponding to the S2 signals from the bottom PMTs). These two quantities can be understood as spatial-averaged signals. For simplicity we use the spatial-averaged gain factors of $g_1 = 0.142$ and $g_2 = 11.4$ for cS1 and cS2_b, respectively. Thus in this case the number of PE is given by $N_{pe} \sim \text{Binom}(N_\gamma, g_1)$ and that of proportional signal is given by $N_{prop} \sim \text{Gauss}(N_e g_2, \sqrt{N_e} \Delta g_2)$, with $\Delta g_2/g_2 = 0.25$. The cS1 and cS2_b signals are constructed from N_{pe} and N_{prop} . The biases and fluctuations in the construction process is modeled as

$$cS1/N_{pe} - 1 \sim \text{Gauss}(\delta_{s1}, \Delta\delta_{s1}),\tag{S-5}$$

$$cS2_b/N_{prop} - 1 \sim \text{Gauss}(\delta_{s2}, \Delta\delta_{s2}),\tag{S-6}$$

where we adopt mean values of $\delta_{s1(s2)} = -0.065$ (0.034), and variances $\Delta\delta_{s1(s2)} = -0.110$ (0.030).

$$\begin{aligned}\langle cS1 \rangle &\approx \frac{T_N \cdot L}{W} \frac{\langle r \rangle + \langle N_{ex}/N_i \rangle}{1 + \langle N_{ex}/N_i \rangle} g_1 \cdot (1 + \delta_{s1}), \\ \langle cS2_b \rangle &\approx \frac{T_N \cdot L}{W} \frac{1 - \langle r \rangle}{1 + \langle N_{ex}/N_i \rangle} g_2 \cdot (1 + \delta_{s2}).\end{aligned}\tag{S-7}$$

In the left panel of Fig. S-2, we show the Monte Carlo (MC) simulation of the signal distributions from a typical scattering between non-relativistic halo DM and xenon nucleus for $m_\chi = 200$ GeV and $\sigma_{\chi p} = 4.7 \times 10^{-47}$ cm². We adopt the Maxwellian distribution of the standard halo model (SHM) for DM with the most probable velocity $v_0 = 220$ km/s, the escape velocity $v_{esc} = 544$ km/s, the local DM density $\rho_\chi^{\text{loc}} = 0.3$ GeV/cm³ and the Earth velocity $v_E = 232$ km/s [74]. We assume the scattering process is elastic, spin-independent and isospin-conserving, and adopt the Helm form factor [44]. We find that the figure is in reasonable agreement with the result of the Xenon-1T collaboration [50].

For deriving the constraints on $\sigma_{\chi p}$ from halo DM, we consider two different two statistic methods. The first one is the Binned Poisson (BP) method [53, 54]. First, Let us consider the single-bin case. Given an expectation value of $\lambda = b + s$ events with s the theoretical prediction and b the expected background, the probability of observing N_{obs} events is given by the Poisson distribution

$$P(N_{obs}|\lambda) = \text{Poiss}(N_{obs}|\lambda).\tag{S-8}$$

The value of λ_p at which $P(\lambda > \lambda_p | N_{obs})$ is smaller than α is excluded at $1 - \alpha$ confidence level (C.L.). For example, the 90% C.L. exclusion limit means $\alpha = 0.1$. The required λ_p can be obtained from $P(\lambda > \lambda_p | N_{obs}) = P(N < N_{obs} | \lambda_p) < \alpha$. In the case of multiple bins, if $(1 - \alpha_{\text{bin}})$ is the probability of seeing $\lambda < \lambda_p$ in that bin, the possibility $(1 - \alpha)$ of seeing $\lambda < \lambda_p$ in any of the bins is given by the binomial distribution

$$1 - \alpha = (1 - \alpha_{\text{bin}})^{N_{\text{bin}}},\tag{S-9}$$

where N_{bin} is the number of bins. For a desired exclusion level of $1 - \alpha$, we then use this relation to determine α_{bin} , and find the value of λ_p .

The second one is the Maximal Likelihood (ML) method. In this method, the joint likelihood is obtained by the product of individual likelihoods in each bin i , i.e., $\mathcal{L} = \prod_i \mathcal{L}_i$ where $\mathcal{L}_i = \text{Poiss}(N_{obs}|\lambda_i)$ is the Poisson distribution. The theoretical prediction of the event number depends on DM parameters, e.g. $\lambda_i = \lambda_i(m_\chi, \sigma_{\chi p})$. The test statistics is defined as

$$\text{TS} = -2 \ln \frac{\mathcal{L}(m_\chi, \sigma_{\chi p})}{\mathcal{L}(\hat{m}_\chi, \hat{\sigma}_{\chi p})},\tag{S-10}$$

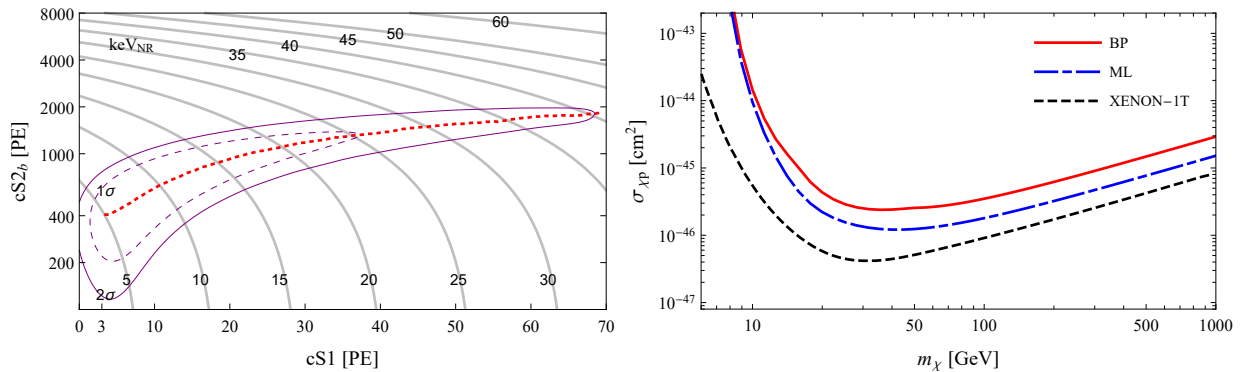


Figure S-2. Left) Nuclear recoil signal distributions from halo DM-Xe scattering with $m_\chi = 200$ GeV and $\sigma_{\chi p} = 4.7 \times 10^{-47}$ cm², through MC simulation. The purple dashed and purple solid are 1σ and 2σ percentiles of DM signal, and the central value (red dashed) is shown for reference. The gray lines are the iso-energy contours in keV_{nr}. Right) 90% C.L. upper limit on $\sigma_{\chi p}$ from DM of SHM by two different statistic approaches described above, binned Poisson (BP, red solid) maximum likelihood (ML, blue dot-dashed). We also show the result from XENON-1T (black dashed) for comparison.

where \hat{m}_χ and $\hat{\sigma}_{\chi p}$ are the best-fit DM parameters which maximize the likelihood. For a given value of m_χ , the TS should approximately follow a χ^2 -distribution with one degree-of-freedom [75]. The value of σ_χ for which TS > 2.7 are excluded at 90% C.L..

For the S1-S2 combined data analysis, the Xenon-1T collaboration adopted the energy regions of interest (ROI) for cS1 as $3 < cS1 < 70$ PE, corresponding to an average energy of 4.9–40.9 keV_{nr}. The ROI for cS2_b is $50.1 < cS2_b < 7940$ PE. The selection of ROIs affects the total acceptance. We take the total acceptance due to the data selection, reconstruction, noise rejection, S1-S2 correlation and single scattering, etc.. from Fig. 14 of [76]. In deriving the constraints on CRDM, we use the data of cS2_b distribution shown in Fig. 4 of [50]. In the figure the distribution is shown with respect to the rescaled quantity $(cS2_b - \mu_{ER})/\sigma_{ER}$, where μ_{ER} and σ_{ER} are the ER mean and 1σ quantile, respectively. We take $\mu_{ER} = 1958$ PE and $\sigma_{ER} = 408$ PE from the cS2_b distribution shown in Fig. 3 of [50]. The number of signal counts s_i in a given bin of cS2_b signal is given by

$$s_i = E_X \int_{(cS2_b)_i^{\text{low}}}^{(cS2_b)_i^{\text{up}}} d\langle cS2_b \rangle \frac{dN}{dT_N} \frac{dT_N}{d\langle cS2_b \rangle} \epsilon_2(\langle cS2_b \rangle), \quad (\text{S-11})$$

where $E_X = 1$ tone · year is the total exposure of the XENON-1T data, $(cS2_b)_i^{\text{low(up)}}$ is the lower (upper) endpoints of the i -th bin of the corresponding cS2_b signal. $\epsilon_2 = A_1(cS1)A_2(cS2_b)$ is the total efficiency of cS2_b, where $A_{1,2}$ are the acceptance within the ROI of cS1 and cS2_b, respectively, and are vanishing outside the ROIs. The value of $\langle cS1 \rangle$ and $\langle cS2_b \rangle$ are related to each other through Eq. S-7, so the total efficiency of S2 can be written as a function of $\langle cS2_b \rangle$ only. For the background event number b_i , we directly adopt the overall expected background given by XENON-1T, which include electric recoils, neutron, surface, accidental coincidence (AC), and coherent elastic neutrino-nucleus scatters (CEνNS).

In the right panel of Fig. S-2 we show the upper limits on $\sigma_{\chi p}$ at 90% C.L. for SHM DM using the BP and ML statistic methods. The DM local density and velocity distribution are the same as that for Fig. S-2. In the figure, the limits obtained by the Xenon-1T collaboration using a full profile likelihood analysis is also shown for comparison. It can be seen that the limits obtained in BP and ML approaches are quite conservative. As we are interested in conservative constraints on CRDM properties, we adopt the BP statistic approach in the main text.

Using the relation between the S2 signal and the averaged recoil energy for NR and ER process shown in Fig. 6 of the supplementary material of [51], we convert the Xenon-1T S2-only data in Fig. 4 Ref. [51] into the NR recoil energy distribution dN/dT_N . The total number of events in the i -th energy bin is given by For s_i , we have

$$s_i = \int_{(T_N)_i^{\text{low}}}^{(T_N)_i^{\text{up}}} dT_N \frac{dN}{dT_N} \epsilon_{\text{ex}}(T_N), \quad (\text{S-12})$$

where $(T_N)_i^{\text{low(up)}}$ is the lower (upper) endpoints of the i -th energy bin, and $\epsilon_{\text{ex}}(T_N)$ is the effective exposure which is a function of recoil energy T_N shown in Fig. 1 of Ref. [51]. For the background event number, we use the expected background given by XENON-1T, which include cathode, CEνNS, flat ER background for S2-only data.

III. EXCLUDED REGIONS FOR CRDM

Making use of the Xenon-1T S1-S2 data, we derive the excluded regions in $(m_\chi, \sigma_{\chi p})$ plane using the BP statistic approach for the four different parametrizations of the primary CR flux. The results are shown in Figure S-3. It can be seen that the constraints based on the ‘‘Global-Fit’’ parametrization is quite conservative compared with other parametrizations.

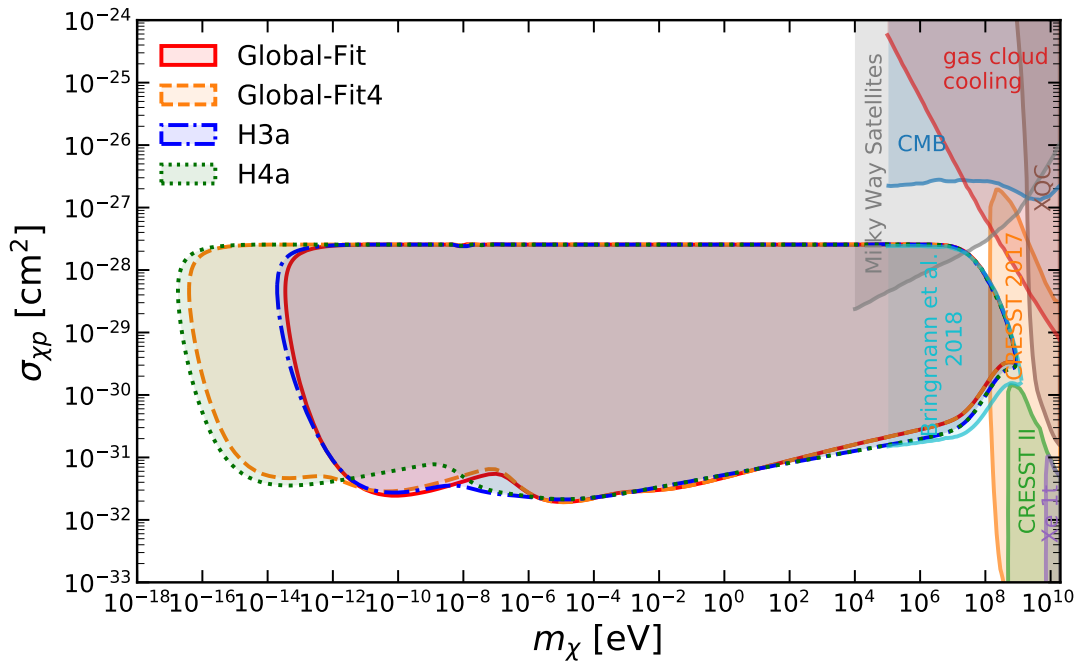


Figure S-3. Exclusion regions in the $(m_\chi, \sigma_{\chi p})$ plane from the Xenon-1T data on the S1-S2 signals and four CR parameterizations.